RESEARCH

CdS Nanoparticles Decorated on Carbon Nanofibers as the First Ever Utilized as an Electrode for Advanced Energy Storage Applications

Muhammad Arif[1,2] · Muhammad Zia Ullah Shah[1,2] · Syed Awais Ahmad[1,2] · Muhammad Sanaullah Shah[1,2] · A. Shah[2] · Ehsan Ullah[1,4] · Taihong Huang[1] · Jianhong Yi[1] · Muhammad Sajjad[3] · Peng Song[1]

Abstract

Electrode material with exceptional durability, energy density, and rate performance has been of great interest in next-generation advanced supercapacitor applications in recent years. In this paper, we portray the facile synthesis of carbon nanofibers (CNFs) and cadmium sulfide (CdS) for a supercapacitor that obtained the capacitances of 335 F/g and 210 F/g when tested in an aqueous conducting medium in a three-electrode mode over a wide potential range between 0.0 to 0.8 V. The performance of pure electrode materials is not satisfactory; therefore, a composite of CdS/CNFs was further fabricated that exhibits enhanced energy storage performance in terms of the capacitance of 510 F/g, and a minor charge transfer resistance compared with pure counterparts. The fascinating performance was turned to develop an asymmetric supercapacitor (CdS/CNFs‖AC), which realizes a high voltage of up to 2.0 V. It is believed that optimization of voltage put significant enhancement in energy and power delivery. Interestingly, a high power of 9000 W/kg was accomplished with maximum energy of 31.94 Wh/kg at high and low discharge current rates. Additionally, only a 15.3% capacity fade was attained and 85.7% retention at a high current rate of 20 A/g for 7500 cycles. Our strategy is synthesizing other metal oxide-based composite electrodes for future energy storage domains.

Keywords Carbon nanofibers · Cadmium oxide · Electrode material · Cycling stability · Power delivery

1 Introduction

Researchers are drawn to supercapacitors (SCs) because of their desirable characteristics, such as their extraordinary power density, long life cycle, rapid charge/discharge rates, and ability to operate safely across a wide range of temperatures [1–6]. Portable electronics, backup power sources, load cranes and forklifts, electric utilities, and hybrid electric vehicles use SCs because of their mentioned features [6–8]. Based on the charge storage technique, Scs are divided into double-layer capacitors (EDLCs) and pseudocapacitors [9–11]. EDLCs are based on materials with a high surface charge separation at the electrode–electrolyte interface region. In contrast, pseudocapacitors were based on the reversible faradaic redox reaction of active species on the electrode surface. Electrodes in Scs are commonly made of three types of materials: carbon materials, metal oxide or hydroxide materials (MnO_2, CuO, Co_3O_4, MoO_3, and Ni $(OH)_2$, and conducting polymers [12–16]. SCs have two key challenges: a low energy density (less than 10 mWh/g) and a high cyclability [17–19]. As a result, novel electrode

✉ A. Shah
  attashah168@gmail.com

✉ Muhammad Sajjad
  sajjadfisica@gmail.com

✉ Peng Song
  songpengkm@163.com

1 Faculty of Materials Science and Engineering, Kunming University of Science and Technology, Kunming 650093, China

2 National Institute of Lasers and Optoelectronics College, Pakistan Institute of Engineering and Applied Sciences, Nilore 45650, Islamabad, Pakistan

3 College of Chemistry and Life Sciences, Zhejiang Normal University, Jinhua 321004, China

4 Faculty of Metallurgical and Energy Engineering, Kunming University of Science and Technology, Kunming 650093, China

materials with high energy density and long cyclability are urgently required.

Individual electrode materials' nanostructure improves electrochemical performance by increasing their energy density. Because of their outstanding properties, recent metal sulfides (MSs) have drawn interest as cutting-edge electrode materials for electrochemical SCs [20, 21]. These characteristics include high specific capacity, low electronegativity, unusual crystal structures, and redox activity [22–25]. Metal sulfides (MSs) have better electrochemical performance than metal oxides (MO's) due to the substitution of oxygen atoms for sulfur atoms. With an alkaline electrolyte, the MSs undergoes a reversible redox reaction. CdS, CuS, ZnS, MoS_2, and CoS have demonstrated significant specific capacitance due to the valence states of materials that improve the device's energy density [26–30].

CdS is one of the outstanding electrode active materials among various sulfides owing to its narrow bandgap of 2.4 eV, fantastic faradaic redox activity, and high conductivity with unique chemical and physical properties [31–39]. Besides, it is well known that the limited irreversible adsorption of ions on the interface between electrolyte/electrode is the leading cause of low capacitance of the carbon materials (herein CNF) [40]. In light of this, developing novel nanostructured electrodes effectively increases the utilization of electrolyte ions. It expands the electrolyte/electrode interface area and short ion/electron transport pathways, boosting the final electrochemical performance of the host active electrode. CdS have been evaluated among several literature reports due to their good electrical conductivity, prolonged life cycle, larger specific area, and cheaper cost. For instance, Xu et al. [41] described a hydrothermal process for producing porous CdS on nickel foam with specific capacitances of 909 F/g at 2 mA/cm². Nisha et al. [1] demonstrate that solvothermal-produced CdS nanosheets have a capacitance of 1165 F/g at 2 mV/s. Zhang et al. formed 3D reduced graphene oxide/CdS hydrogels with specific capacitances of 300 F/g at 5 mV/s for SCs [42]. At a scan rate of 5 mv, the observed CdS microspheres [43] had a specific capacitance of 592 F/g. The theoretically measured specific capacitance value of CdS is 1675 F/g, although empirically obtained capacitance values of CdS are substantially lower. This difference between theoretical and actual values encourages researchers to devise novel methods for fabricating CdS-based SCs.

The specific capacitance and energy density must be progressively enhanced to fulfill the expanding energy needs. The CNF's double-layer capacitance and the CdS faradaic capacitance may improve the electrode's electrochemical characteristics. CNFs have piqued the interest of researchers because of their outstanding conductivity and thermal and chemical stability [44–46]. As the electrode material in a supercapacitor, CNFs have a high working voltage, appealing life duration, and excellent capacity retention [47, 48].

Given the above explanation, we have manufactured CdS and CNF nanoparticles using a simple Co-precipitation technique and hydrothermal process, respectively. CdS-CNFs nanocomposite was prepared by wet chemical process to examine their performance as a supercapacitor electrode material. CdS nanoparticles assembled into CNFs enhanced the performance of a composite material. These composite materials offer several advantages. First, the fiber-shaped porous carbon has a high aspect length-to-volume ratio and a condensed ion/electron diffusion channel, allowing for quick electron transport and the necessary electrochemical performance. Second, Cadmium was uniformly distributed over the carbon matrices to meet the critical requirements in SCs. We describe a novel possibility and prospective electrode materials for enhanced SCs, which, to the author's knowledge, have not been previously reported.

2 Synthesis of the Samples

2.1 Materials and Methods

Analytical-grade chemicals were employed to make composite CdS-CNFs and CdS, and they were used directly after production. Cadmium acetate ($C_4H_6CdO_4$, 97%) and elemental Sodium Sulfide Hydrate ($Na_2S \cdot 9H_2O$) were supplied from Sigma–Aldrich. Every single stock solution was made with deionized (DI) water. Resorcinol (99.5%), hexamethylene tetramine (HMT), cetyltrimethyl-ammonium bromide (CTAB) (99%), tetraethyl orthosilicate (TEOS), NaOH, and ammonia solution (25%), were all supplied by Sinopharm Chemical Reagent Co., Ltd. Fluka provided the Pluronic F127. The sulfur (> 99.99% purity) came from Aldrich.

2.2 Synthesis of CdS NPs via Co-precipitation Technique

For the synthesis of CdS nanoparticles, the facile-precipitation technique has been used. In a typical synthesis, Cadmium acetate 0.2 M is dissolved in 100 ml DI water and ethanol. Sodium sulfide ($Na_2S \cdot H_2O$) 0.2 M dissolved in 100 ml DI water and ethanol. During stirring, dropwise added sodium sulfide solution in Cd acetate solution. After mixing solution was further started at 70 °C for 80 min. Then the solution was filtered and washed with ethanol and DI water several times and dried up in an oven at 80 °C for 30 min. The product was annealed at 500 °C for 2 h to remove impurities.

Table 1 Demonstrates CdS-CNFs nanocomposites with various weight percentages

Samples	Composition	Pure CNFs (g)	Pure CdS (g)	Methanol (mL)	Time (h)	Temp (°C)
CdS-CNFs	CdS-CNFs (30–70) %	0.56	0.24	40	18	80°

2.3 Preparation of Carbon Nanofibers

Polymer nanofibers were generated via the hydrothermal synthesis of R (2.5 mmol) and HMT (1.5 mmol) with surfactant F127 at 110 °C for 4 h. The polymer product (PNFs) was subsequently washed with water three times. PNFs were pyrolyzed for 2 h at 600 °C in a nitrogen atmosphere to produce microporous carbon nanofibers (CNFs).

2.4 Preparation CdS-CNFs Composites

Wet chemical methods were used to generate CdS-CNFs nanocomposites. The percent combinations for CdS and CNFs are 30% to 70%, respectively. For each variety, 40 mL of methanol was added. The solution was then subjected to 40 min of sonication. For 40 min, magnetic stirring was utilized to ensure the solution was completely dissolved. The solvent was then removed from the mixture by heating it to 80 °C for 18 h (Table 1).

2.5 Characterization

Electron microscopy was used to analyze the structural morphology of pure and composite materials (FESEM,

Table 2 The lattice strain and grain size were calculated from the Scherrer formula

Samples	Avg FWHM	AVG grain size (nm)	Avg lattice strain (ε_{strain})
CdS	0.5185	20.8	0.5813
CNFs	0.3351	51.2	2.3304
CdS-CNFs	0.3667	25.1	0.4987
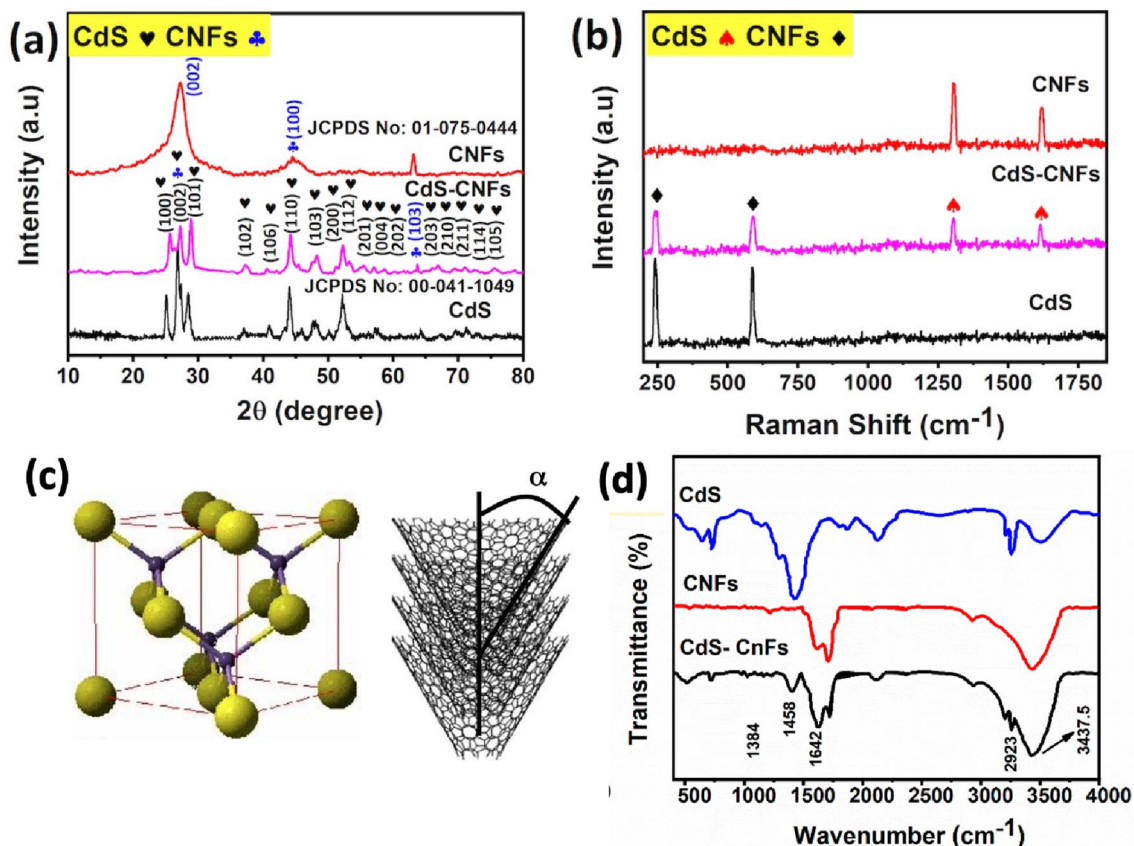
Fig. 1 **a** XRD pattern, **b** Raman analysis, **c** the unit cells of CdS and CNF, and **d** FTIR spectra of the CdS, CNFs, and CdS-CNFs samples

TESCAN Mira3, Czech Republic). A thermal scientific manufactured XRD (EQUINOX 3000) X-ray diffractometer with Cu Kα radiation (λ = 1.54056 A°) was used to evaluate the crystal structure and phase purity. It was set at 40 kV and 40 mA, respectively, for the X-ray source's working voltage and current. Raman spectroscopy investigated the samples' vibrational modes (Model, Dongwoo Optron Co. Ltd). Composites were micro-structured using the field-emission scanning electron microscope (TESCAN built FE-SEM, model: MAIA-3). The Octane Elite detector can also analyze the sample's elemental appearance. The electrochemical characteristics of the nanocomposite samples were evaluated using an electrochemical workstation (Gammry101). Tests on the electrodes included cyclic voltammetry (CV), galvanostatic charge–discharge (GCD), electrochemical impedance spectroscopy (EIS), and cycle life measurements.

2.6 Electrochemical Measurement

It was combined with conductive carbon (10%), active material (80%), and polyvinylidene fluoride (PVDF) as a binder (10%) in N-methyl-2-pyrrolidone (NMP) solvent to form a viscous slurry, which was then utilized to manufacture the active electrode material. This slurry served as the working electrode after being coated on a 1×2 cm^2 patch of carbon sheet and dried at 70 °C overnight. For electrochemical studies in a three-electrode configuration with a 3 MKOH aqueous solution in the 0 to 0.8 V potential range, the reference electrode is Ag/AgCl. In contrast, the counter electrode is a platinum wire. CV and GCD tests were performed on the synthesized materials and composites using a voltage range of 0.0 to 0.8 V, and an EIS was acquired using the same instrument at frequencies ranging from 0.1 to 100 kHz. Cycling's consistency of up to 10,000 charge–discharge cycles was evaluated at a current density of 5 A/g. Consequently, the platinum foil was employed as a counter electrode, and Ag/AgCl was used as a reference electrode [49].

$$\frac{m+}{m-} = \frac{C-}{C+} \times \frac{V-}{V+} \qquad (1)$$

The above formula represents the relationship between the anode and cathode masses (m_+/m_-), the capacitance and potential difference (C_-/C_+), and the voltage between the anode and cathode (V_-/V_+) [28, 50].
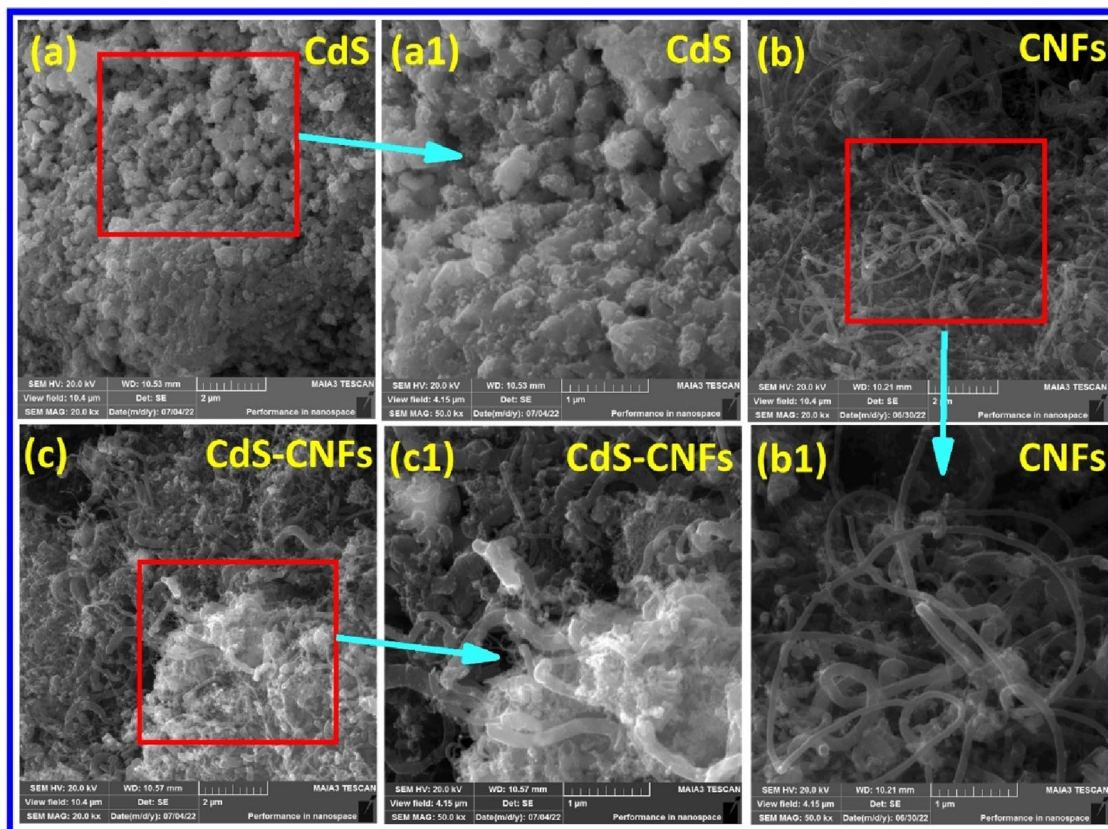

Fig. 2 The SEM images of **a**, **a1** CdS, **b**, **b1** CNFs, and **c**, **c1** CdS-CNFs composite

$$C_s = \frac{I \times \Delta t}{m \times \Delta V} \tag{2}$$

$$E = \frac{Cs \times \Delta V^2}{7.2} \tag{3}$$

$$P = \frac{3600 \times E}{\Delta t} \tag{4}$$

where Δt is the discharge time, Δv denotes the potential difference; Cs is the capacitance, m+ and m− are the masses of the positive and negative electrodes, and C+ and C− are the capacitances, respectively.

3 Results and Discussion

XRD diffractogram analysis was used to analyze the samples sufficient and successful formation in terms of their structure, phase purity, and crystallinity. The XRD peaks of the synthesized samples are seen in Fig. 1a. In the XRD pattern of pure CNFs, significant peaks at $2\theta = 15.7°$, 21.7°, and 37.5° were seen [1]. The reflections from the planes (110) (002) and have these angles as their respective (004). Peaks at 2 values of 24.9°, 26.6°, 28.3°, 36.8°, 43.9°, 51.1°, 52.1°, 53.1°, 54.9°, 67.1°, 69.6°, 71.2°, 72.8°, and 75.9° are shown in X-ray diffraction patterns for CdS nanoparticles and are in good agreement with the (100), (002), and (101). Doping usually induces some lattice deformation and would thus lead to peak intensity decreases of the CdS-CNFs. All peaks correlate well with the previous study and demonstrate that the absence of impurity peaks in either pattern showed the exceptional purity of the products. The unit cell of the ZnO and CNFs active materials are depicted in Fig. 1c, leading to their respective crystal structures. The crystallite sizes of the CNFs nanomaterials are computed using the Scherrer Eq. (5), and the crystallite size of these materials was determined to be around 51.2 nm.
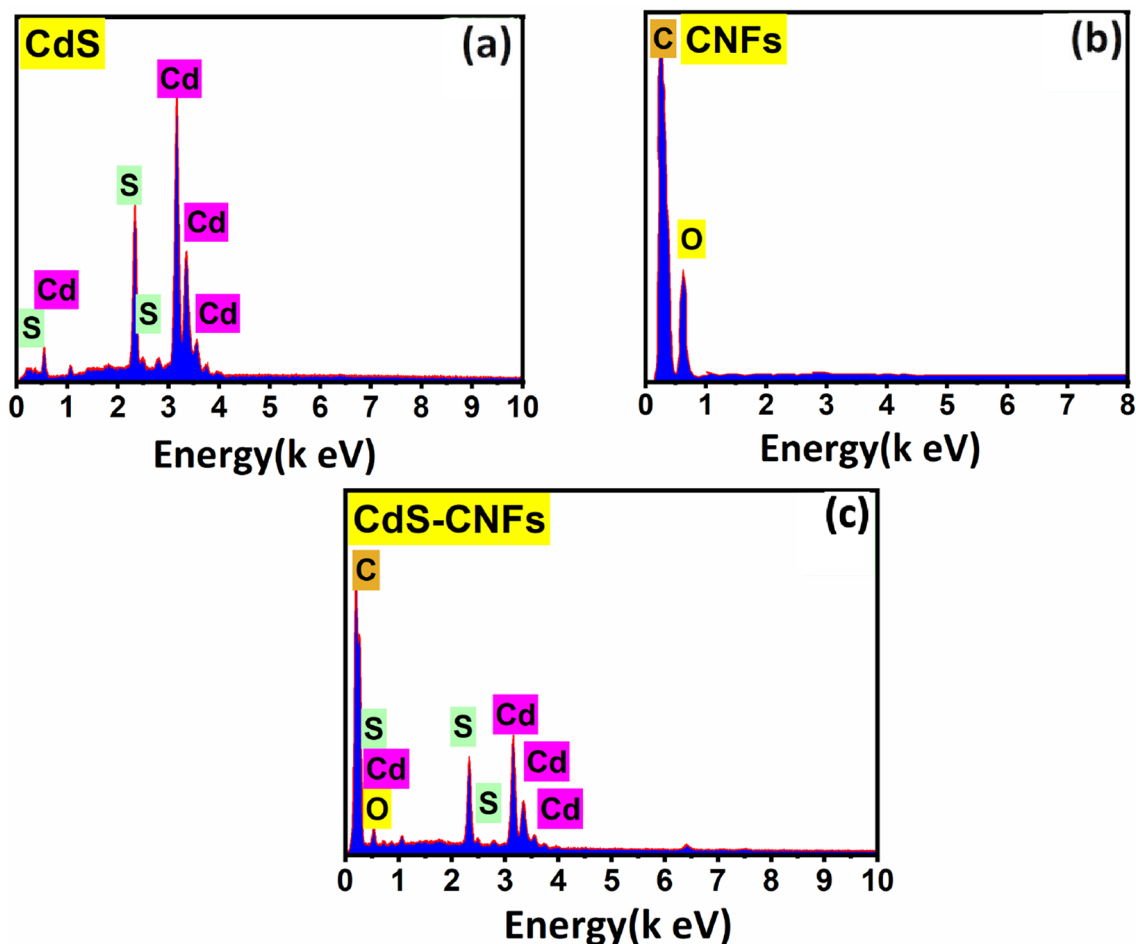

Fig. 3 The EDX images of **a** CdS, **b** CNFs, and **c** CdS-CNFs composite
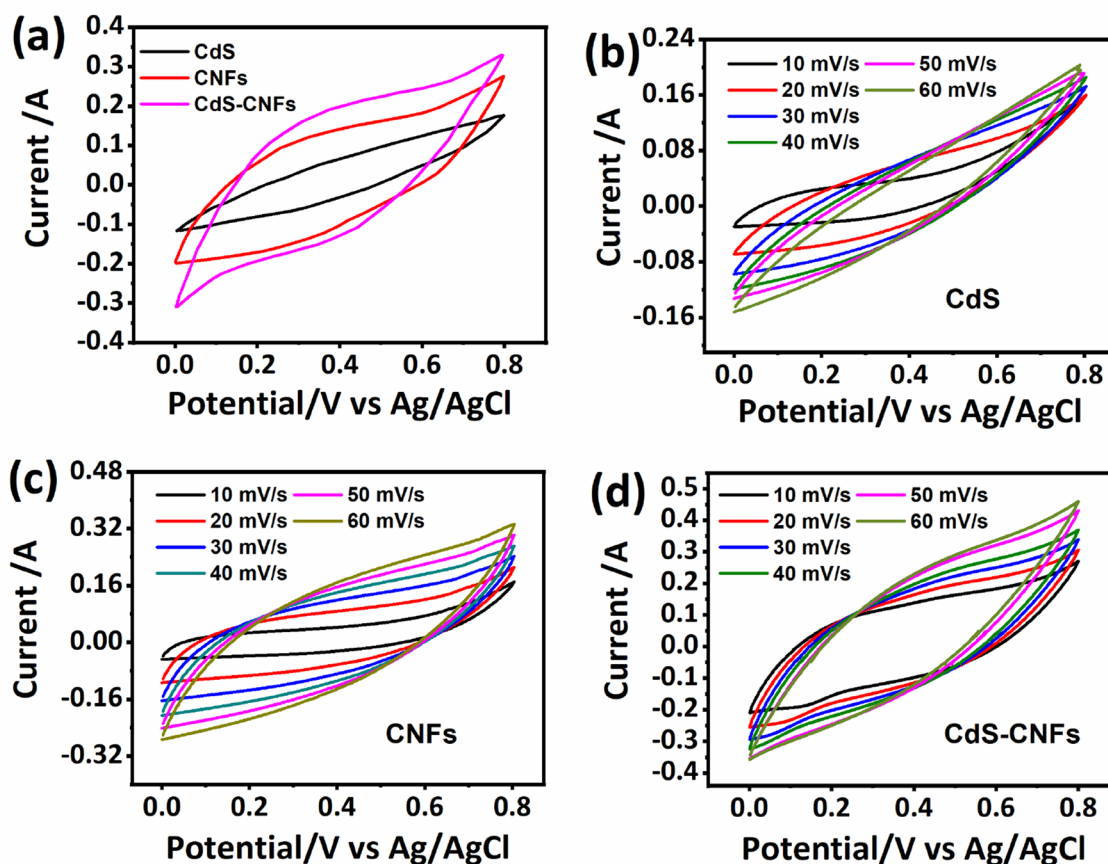
Fig. 4 **a** The CV voltammogram of all electrodes at a fixed scan, **b–d** CV curves of CNFs, CdS, and CdS-CNFs composite electrodes at identical conditions

$$D = 0.94\lambda/\beta cos\theta \qquad (5)$$

β represents the full width at half maximum, θ denotes Bragg's angle, and CuKα λ = 0.154 nm denotes X-ray wavelength. The crystal sizes of the CdS nanomaterials are calculated, in which the crystal size of 20.8 nm and their nanocomposite crystal size changes concerning CNFs weight percentage value shown in Table 2.

At room temperature, the Raman spectra of CdS nanocrystals are shown in Fig. 1b. Raman spectra were taken under natural circumstances further to study the structural information of pure CdS and CNFs. The results of these investigations are depicted in Fig. 1b. The advancement in the longitudinal optical (LO) phonon mode is the dominant feature in these Raman spectra. Every spectrum has a peak on both ends. The primary E_2 vibrational mode produces the Raman signal measured at 244 cm^{-1}. The scattering 2 LO phonons of CdS are responsible for the peak at 596 cm^{-1} [51]. The CNFs have substantial rises at 1325 cm^{-1} and 1612 cm^{-1}, which correlate to the D and G. Because of near-resonant scattering, the time required to get a measurement is two to three orders of magnitude less than it would be

under green excitation circumstances. In other words, the time needed to acquire a measure is seconds rather than minutes.

The structure of molecules and composition of the molecular mixture confirmation were additionally examined by taking the Fourier to transform infrared spectroscopy (FTIR) analysis, as demonstrated in Fig. 1d. Apparently, the CdS shows a weak peak at 654 cm^{-1} that can be assigned to the C–H stretching, and 1394 cm^{-1} due to O–C=O asymmetric stretching, respectively. The peak at 3460 cm^{-1} is due to the –OH stretching of water molecules adsorbed on the surface of the CdS. The bands at 1040 cm^{-1}, (C–O stretching with primary alcohol), 1116 cm^{-1} (C–O stretching of secondary alcohol), 1642 cm^{-1} (C=C stretching), 2923 cm^{-1} (C–H stretching band), and 3437.5 cm^{-1} corresponds to the hydrogen bonding, respectively. The CNF reflected several peaks at 3436 cm^{-1} and 1384 cm^{-1} that are associated with the –OH stretching and bending mode, respectively, indicating the presence of a –OH functional group on CNF. Moreover, the CdS-CNF composite reveals the vibrational stretching mode at 2923 cm^{-1}, 2854 cm^{-1} (C–H stretching from aldehyde), 1706 cm^{-1} (C=O stretching mode), 1622 cm^{-1}
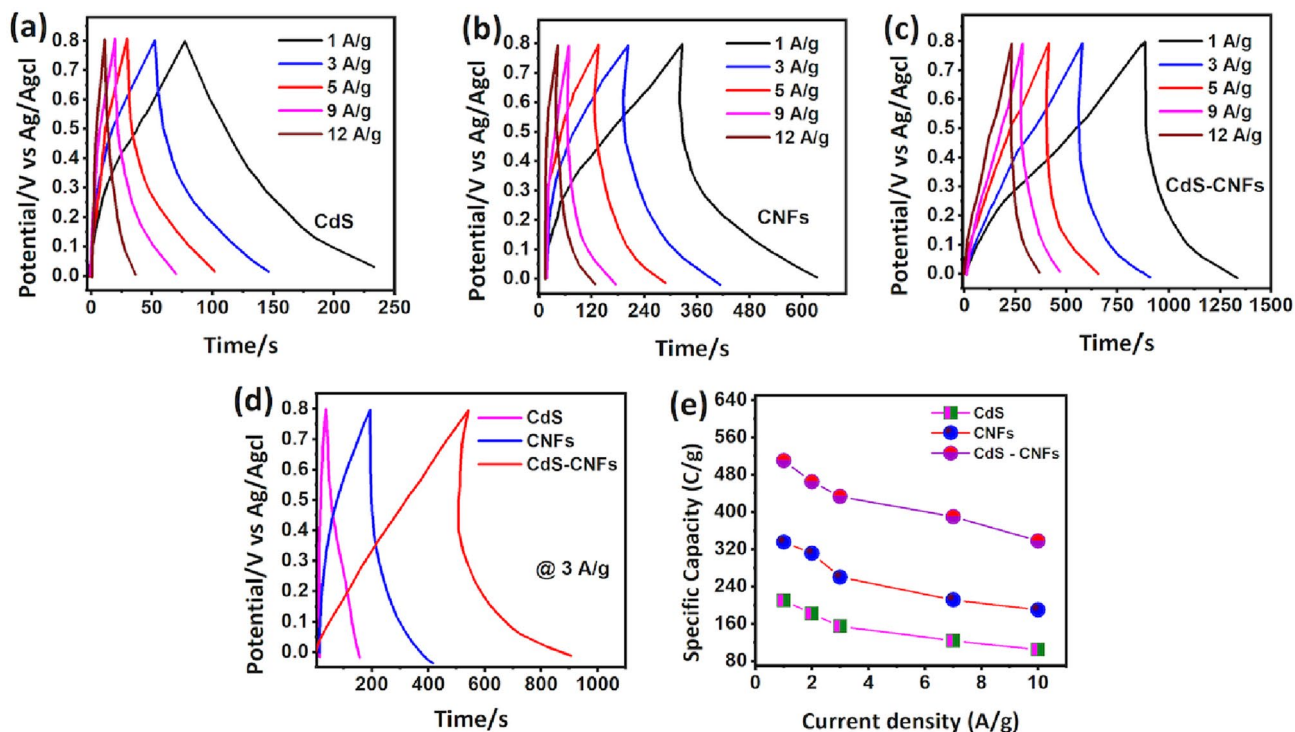
Fig. 5 **a–c** The discharge/charge profile of CNFs, CdS, and CdS-CNFs composite electrodes at identical current rates, **d** comparative discharge/charge plots at fixed current, **e** capacitance plot w.r.t discharge current density

Table 3 Discharge currents and the capacitance of individual electrode material

Current density (A/g)	CdS (F/g)	CNFs (F/g)	CdS-CNFs (F/g)
1	210	335	510
3	182	311	465
5	155	260	433
9	124	212	390
12	105	190	338

(C=C), 1216 cm^{-1}, (C–O from the alkyl aryl ether) and 1384 cm^{-1} (O–H bonding phenol).

The morphology of the samples was explored by FESEM analysis. The CdS sample validates the morphology composed of clusters of nanoparticles with aggregation (Fig. 2a, a1). The bundles and aggregated morphology of the CNFs were distinguished and presented in Fig. 2b, b1. Meanwhile, the CdS-CNFs composite displayed a combined effect of nanoparticles and CNFs, indicating the adequate preparation of the products that can be clearly shown in Fig. 2c, c1. In all products, no extra residence was observed on the surface sign towards the high purity of the samples.

To further support the XRD and FESEM results, EDX analysis was taken for sample purity and compositional

confirmation. Figure 3 presents the EDX spectra of all samples. All samples depicted the peaks of only their respective elements without any additional peaks from impurity/by-products, confirming the purity and well formation of the pure CdS, CNFs, and their composite (Fig. 3a–c), respectively.

The electrodes' energy storage performance and capacitive behavior were individually investigated using electrochemical analysis techniques, such as CV voltammogram chronopotentiometry via discharge/charge profile and an impedance technique. The voltammogram of CdS, CNFs, and CdS-CNFs electrodes in a potential region between 0.0 to 0.8 V is presented in Fig. 4. The comparative voltammogram of CdS, CNFs, and CdS-CNFs composite electrodes at identical condition is provided in Fig. 4a, which signifies that the CdS-CNFs composite encloses the highest loop area under the CV curve at fixed sweep rate, signing towards the highest capacitance. The pear-shaped CV curves outlined the collective behavior of the CdS (pseudocapacitive) and CNF (double-layer capacitive) in the composite electrode. Subsequently, the capacitive performance of individual electrodes is further assessed to know their energy storage fashion in-depth. As demonstrated in Fig. 4b, the CV voltammogram of the CdS electrode reveals an oval-type shape, confirming the pseudocapacitive behavior. It was observed that from high to low scanning, the formation of the CV
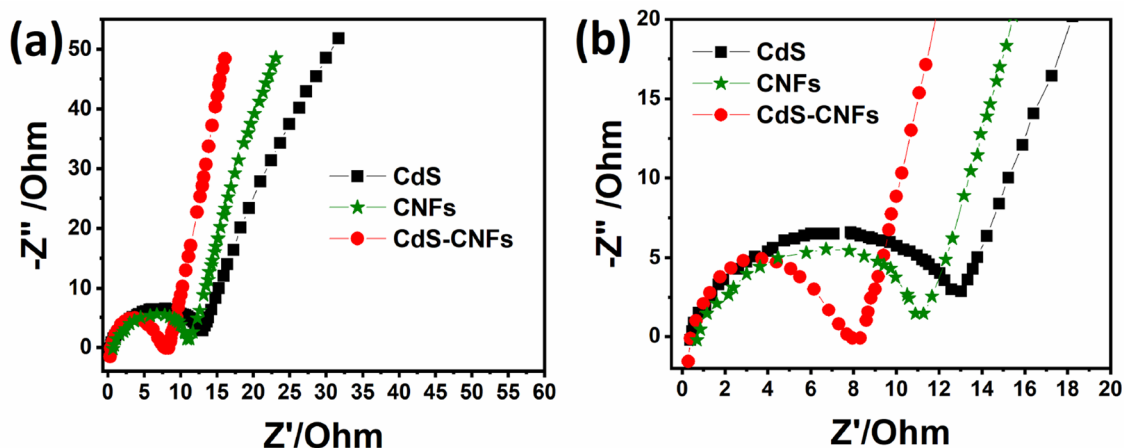
Fig. 6 The impedance spectroscopy plot of CdS, CNFs, and CdS-CNFs composite electrodes at low (**a**) and enlarged view (**b**)

Table 4 The impedance plot parameters

Sample	CdS	CNFs	CdS-CNFs
Rs	0.05	0.04	0.01
Rct	12.8	10.9	8.1

loops sustained, specifying the typical capacitive behavior [49, 52, 53]. Moreover, the CV curves of the CNF electrode showed an almost rectangular shape, which is due to the double-layer charge storage mechanism (Fig. 4c). A similar trend was also observed as scan rate upsurges; no noticeable difference in the CV loops was detected, and mirror images in positive and negative potential, leading to the excellent capacitive behavior and good reversibility of the CNF electrode [54]. The CV voltammogram of the CdS-CNFs composite electrode showed the combined effect in their respective CV loops (pseudocapacitive and double-layer behavior), as depicted in Fig. 4d. The only difference in all electrodes CdS, CNF, and CdS-CNFs composite is that the CdS-CNFs composite encloses the highest current response, resulting in a more extensive loop area than CdS, and CNF, indicating highest capacitance. The chronopotentiometry analysis can further prove this in the next paragraph.

Table 5 Capacitance, energy, and power density at different current rates

Current density (A/g)	1	2	3	5	9
Specific capacitance (F/g)	57.5	47	42	37.5	31.5
The energy density (Wh/kg)	31.94	26.11	23.3	20.83	17.5
Power density (W/kg)	999	1999	2995	4872	9000

The chronopotentiometry technique was employed to measure the discharge/charge characteristic for energy storage evaluation of the CdS-based CNF electrodes in a similar potential regime as already discussed in the CV measurements. For more elaborately, a 0.0 to 0.8 V potential with disparate current rates from 1 to 12 A/g for all electrodes, as given in Fig. 5a–d. The discharge/charge shape of the CdS, CNFs, and CdS-CNFs composite electrodes are schematically provided in Fig. 5a–c. According to Fig. 5a, the CdS electrode typically shows the pseudocapacitive charge storage properties with usual non-linear discharge/charge shape from low to higher current rates, denoting the incredible rate and energy storage performance. Meanwhile, the CNF electrode also showed a mirror shape of the discharge/charge shape, indicating good reversibility and power delivery (Fig. 5b). Furthermore, the CdS-CNFs composite electrode showed a considerable discharge time than CdS and CNF electrodes (Fig. 5c). The comparative discharge/charge plots are presented in Fig. 5d at a fixed discharge current of 3 A/g, showing a large capacitance of the CdS-CNFs composite electrode than CdS, and CNFs electrodes. The capacitance of all electrodes is shown in Fig. 5e, which demonstrates the CdS-CNFs composite electrode is at the top. The capacitance is calculated in Eq. (2). Their values at desired current rates are comprehensively outlined in Table 3.

The impedance spectroscopy was further assessed to know the outstanding performance of the CdS, CNFs, and CdS-CNFs composite electrodes via charge transport kinetic behavior. Figure 6 displayed the impedance plots of all electrodes, which consisted of real and imaginary parts. The x-intercept at the real axis denotes the solution resistance (Rs), and the diameter of the semi-circle presents the charge transfer resistance (Rct). However, the vertical line at the
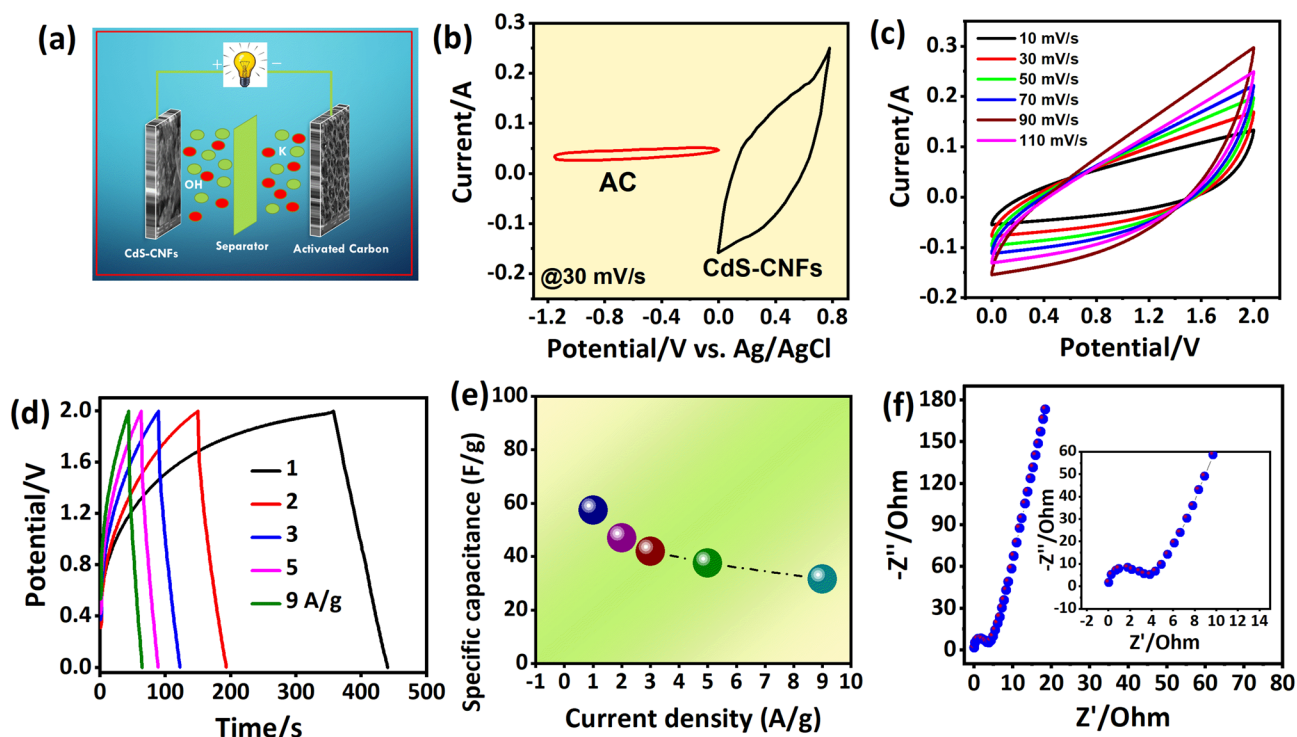
Fig. 7 **a** schematic of the CdS-CNFs‖AC asymmetric SC, **b** potential regime of the AC and Cd-CNFs electrodes, **c**, **d** CV, and discharge/charge shape at various scans and current rates, **e** capacitance plot, and **f** impedance plot, (inset) the zoomed view

Table 6 CdS-CNFs‖AC asymmetric SC performance compared with previous literature with similar electrode materials

Electrode materials	Techniques	Voltage	Specific capacitance (F/g)	Energy density (Wh/kg)	Power density (W/kg)	Cycling stability (%)
NiO/C@CNF//AC [63]	Hydrothermal	0−1.5	742.2	58.43	1947	88%@5 K
CNF/MnO$_2$// [64]	Carbonization	−0.2−0.8	228	25.3	–	94% @10 k
CNF/GN//AC [65]	Facile and cost-effective	0−1.8	178	20	900	–% @ 1 K
Co$_3$O$_4$@CdS SHSC [66]	Hydrothermal	−0.4−0.6	99	40	6500	92%@ 2 K
ZnO–ZnS–CdS//AC [67]	Hydrothermal–	0−1.8	137	36	5422	91%@ 8 K
Ni$_3$S$_2$@CdS//C [17]	Hydrothermal	0−0.5	552	127.5	10,000	90.5%@10 K
CdS-CNFs//AC (This work)	Hydrothermal	0–2	57.5	31.94	9000	85.7%@7.5 K

vertical axis manifests the diffusion resistance of the electrolyte [55, 56]. Based on the impedance plots of CdS, CNFs, and CdS-CNFs, composite electrodes (Fig. 6a) followed a similar trend. The difference is that the CdS-CNFs composite electrode showed smaller Rct and Rs values (see Table 4) than their pure CdS. CNF electrodes (Fig. 6b). The higher Rct values prove the higher conductivity of the composite electrode after the addition of CNF with CdS [57]. The pure CdS electrode reveals higher Rct and Rs values, which signifies the low conductivity and higher electrode/electrolyte interface [58, 59]. On the contrary, as discussed previously,

the CNF electrode shows relatively more minor resistances than the CdS electrode, demonstrating higher conductivity and improved capacitance performance.

The suitability of the synthesized electrodes in real-world applications, the two-electrode mode, is highly desirable. Inspired by the CdS-CNFs composite electrode's fantastic electrochemical performance, we assembled an asymmetric supercapacitor (CdS-CNFs‖AC) using an aqueous conducting medium of 3 M KOH as the electrolyte. The schematic of the assembled CdS-CNFs‖AC asymmetric SC is given in Fig. 7a. The CV curves were
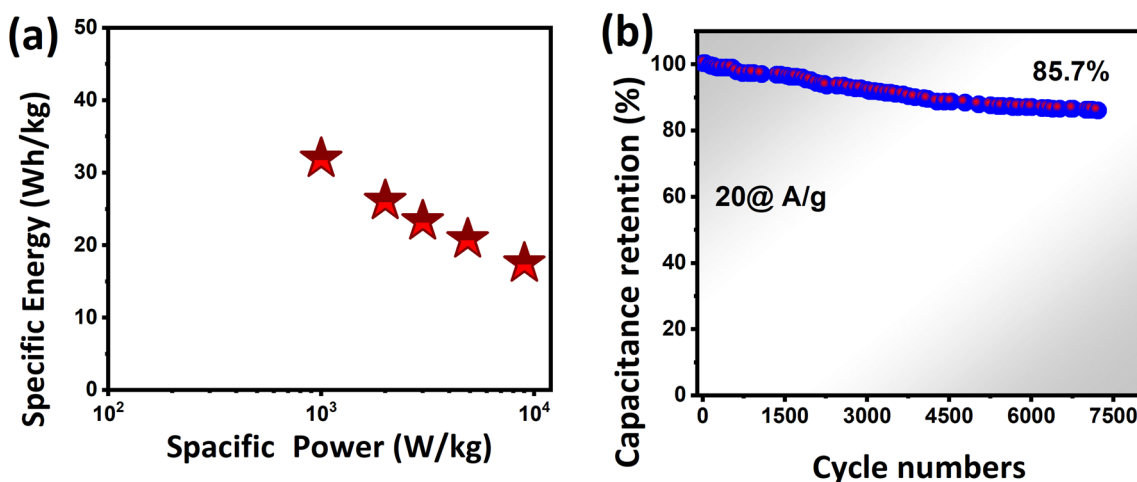
Fig. 8 **a** Ragone plot, **b** stability test of the CdS-CNFs‖AC asymmetric SC

taken at two different potential frames for AC and CdS-CNFs electrodes (− 1.2 to 0.0 V and 0.0 to 0.8 V) to construct an asymmetric supercapacitor (Fig. 7b) up to 2.0 V voltage. The voltammogram of the assembled CdS-CNFs‖AC asymmetric SC was further taken to prove the chosen electrode material is a suitable candidate to fabricate an asymmetric SC. The CV curves revealed the voltage limit reached 2.0 V, meaning that the selected voltage is the well-chosen voltage window. From higher to low scans, the voltammogram is a mirror image at positive and negative potentials, specifying the good reversibility and rate capability of the CdS-CNFs‖AC asymmetric SCs [59]. The discharge/charge feature of the CdS-CNFs‖AC asymmetric SC is displayed in Fig. 7d at various current rates at 0.0 to 2.0 V. A capacitance of 57.5 F/g is determined at 1 A/g, which continually declined and till reached to 31.5 F/g at the upsurge of the current discharge rate of 9 A/g, as depicted in Fig. 7e. The other values at a desired current rate are listed in Table 5. The high capacitance can be due to the high conductive support of the AC and CNF. The impedance plot is further measured to know the supreme performance of the CdS-CNFs‖AC asymmetric SC, as shown in Fig. 7f. A Rs of 0.3 and the Rct value of 3.8 ohms, indicating the high conductivity of the CdS-CNFs‖AC asymmetric SC [60], resulting in enhanced capacitance, as shown in the inset of Fig. 7f.

The energy and power density are the two crucial factors to evaluate the practical aspect of CdS-CNFs‖AC asymmetric SC. The factors are calculated based on the Eqs. (3), and (4). A high energy density of 31.94 Wh/kg and a power delivery of 999 W/kg were attained at 1 A/g, and these values reached 17.5 Wh/kg and 9000 W/kg at the maximum discharge current of 9 A/g. The exact values are listed in Table 6 with their respective current rates. The obtained energy and power delivery confirm the synergy between

CNF and CdS in a composite matrix that sustains a high conductivity due to carbon materials [3, 61, 62]. These values are much higher than the previous literature reports, as tabulated in Table 6. Another essential parameter that accounts for the practical aspect is the cycling stability of the CdS-CNFs‖AC asymmetric SC, which needs to be judged. In this regard, the longevity of the CdS-CNFs‖AC asymmetric SC was tested for 7500 cycles at higher current rates, as presented in Fig. 8b. The continuous was noticed, which may be due to the structural collapse during the electrochemical process. till 7500 cycles, retention of 85.7% at a much higher current rate, demonstrating the excellent cycling stability of the CdS-CNFs‖AC asymmetric SC.

4 Conclusion

A CdS, CNFs, and their combination (CdS-CNFs composite) were prepared by simple hydrothermal route to explore their charge storage performance for asymmetric SC applications. The resulting investigations based on the CV voltammogram, and discharge/charge, reveal an excellent capacitive signature and reversibility combined with full access of the ions to the host electrodes/electrolyte interface, leading to improved performance. The impedance spectroscopy results manifest the rapid charge transfer kinetic with a low charge transfer and solution resistance of the CdS-CNFs electrode material. Afterward, an asymmetric SC (CdS-CNFs‖AC) was assembled, exhibiting good stability of 85.7% (20 A/g) when cycled for 7500 cycles. Not only that, high power was delivered at 9000 W/kg at 17.5 Wh/kg, and when the energy density reached its highest value of 31.94 Wh/kg, a power of 999 W/kg was still delivered. These fascinating results are realized after adding a high voltage of 2.0 V by contacting an asymmetric supercapacitor using an

aqueous medium. Thus, our results confirm that aqueous-based energy storage systems are simple and efficiently utilized to obtain optimized energy storage performance.

Supplementary Information The online version contains supplementary material available at https://doi.org/10.1007/s10904-023-02548-5.

Author contributions Muhammad Arif: wrote the original manuscript draftMuhammad Zia Ullah Shah, Ehsan Ullah, Muhammad Sand Ullah Shah, Syed Awais Ahmad, Taihong Huang, and Jianhong Yi: Prepared all figures with high quality; Data curation; Samples analysisMuhammad Sajjad: Write-Review and EditingA. Shah: Characterization of the samples, e.g., XRD, FESEM, Raman, EDXPeng Song: Supervision

Declarations

Competing interests The authors declare no competing interests.

References

1. V. Nisha et al., CdS nanosheets as electrode materials for all pseudocapacitive asymmetric supercapacitors. Bull. Mater. Sci. **44**(2), 1–7 (2021)
2. N. Nair, S. Majumder, B.R. Sankapal, Pseudocapacitive behavior of unidirectional CdS nanoforest in 3D architecture through solution chemistry. Chem. Phys. Lett. **659**, 105–111 (2016)
3. M. Sajjad et al., Phosphine-based porous organic polymer/rGO aerogel composites for high-performance asymmetric supercapacitor. ACS Appl. Energy Mater. **4**(1), 828–838 (2021)
4. J. Ismail et al., Comparative capacitive performance of MnSe encapsulated GO based nanocomposites for advanced electrochemical capacitor with rapid charge transport channels. Mater. Chem. Phys. **284**, 126059 (2022)
5. B.A. Khan et al., NiSe$_2$ nanocrystals intercalated rGO sheets as a high-performance asymmetric supercapacitor electrode. Ceram. Int. **48**(4), 5509–5517 (2022)
6. X. Zhao et al., Covalent organic framework templated ordered nanoporous C60 as stable energy efficient supercapacitor electrode material. Carbon **182**, 144–154 (2021)
7. S.-J. Bao et al., Biomolecule-assisted synthesis of cobalt sulfide nanowires for application in supercapacitors. J. Power Sources **180**(1), 676–681 (2008)
8. J. Wang et al., Pseudocapacitive contributions to electrochemical energy storage in TiO$_2$ (anatase) nanoparticles. J. Phys. Chem. C **111**(40), 14925–14931 (2007)
9. M.Z.U. Shah et al., A novel TiO$_2$/CuSe based nanocomposite for high-voltage asymmetric supercapacitors. J. Sci. Adv. Mater. Dev. **7**(2), 100418 (2022)
10. M.Z.U. Shah et al., Hydrothermal synthesis of ZnO@ ZnS heterostructure on Ni foam: a binder free electrode for high power and stable hybrid supercapacitors. Mater. Lett. **326**, 132910 (2022)
11. M. Sajjad et al., A review on selection criteria of aqueous electrolytes performance evaluation for advanced asymmetric supercapacitors. J. Energy Storage **40**, 102729 (2021)
12. Q. Yang et al., MXene/graphene hybrid fibers for high performance flexible supercapacitors. J. Mater. Chem. A **5**(42), 22113–22119 (2017)
13. Y. Xie et al., Metal cation substitution of halide perovskite nanocrystals. Nano Res **15**, 6522–6550 (2022)
14. G.F. Chen et al., Polypyrrole Shell@ 3D-Ni metal core structured electrodes for high-performance supercapacitors. Chem. Eur. J. **21**(12), 4614–4621 (2015)
15. G.-F. Chen et al., Hierarchical polypyrrole based composites for high performance asymmetric supercapacitors. J. Power Sources **283**, 484–493 (2015)
16. M.Z.U. Shah et al., A new CuO/TiO$_2$ nanocomposite: an emerging and high energy efficient electrode material for aqueous asymmetric supercapacitors. J. Energy Storage **55**, 105492 (2022)
17. X. Wang et al., High capacitance and rate capability of a Ni$_3$S$_2$@ CdS core–shell nanostructure supercapacitor. J. Mater. Chem. A **5**(15), 7165–7172 (2017)
18. M.Z.U. Shah et al., Copper sulfide nanoparticles on titanium dioxide (TiO$_2$) nanoflakes: a new hybrid asymmetrical Faradaic supercapacitors with high energy density and superior lifespan. J. Energy Storage **55**, 105651 (2022)
19. M. Sajjad, F. Cheng, W. Lu, Research progress in transition metal chalcogenide based anodes for K-ion hybrid capacitor applications: a mini-review. RSC Adv. **11**(41), 25450–25460 (2021)
20. B. Pant, N.A.M. Barakat, H.R. Pant, M. Park, P.S. Saud, J.W. Kim, H.Y. Kim, Synthesis and photocatalytic activities of CdS/TiO$_2$ nanoparticles supported on carbon nanofibers for high efficient adsorption and simultaneous decomposition of organic dyes. J. Colloid Interface Sci. **434**, 159–166 (2014)
21. B. Pant et al., Carbon nanofibers wrapped with zinc oxide nanoflakes as promising electrode material for supercapacitors. J. Colloid Interface Sci. **522**, 40–47 (2018)
22. P. Geng et al., Transition metal sulfides based on graphene for electrochemical energy storage. Adv. Energy Mater. **8**(15), 1703259 (2018)
23. X.Y. Yu, X.W. Lou, Mixed metal sulfides for electrochemical energy storage and conversion. Adv. Energy Mater. **8**(3), 1701592 (2018)
24. X. Rui, H. Tan, Q. Yan, Nanostructured metal sulfides for energy storage. Nanoscale **6**(17), 9889–9924 (2014)
25. M. Sajjad, Recent advances in SiO2 based composite electrodes for supercapacitor applications. J. Inorg. Organomet. Polym. Mater. **31**(8), 3221–3239 (2021)
26. N. Nair, B.R. Sankapal, Cationic-exchange approach for conversion of two dimensional CdS to two dimensional Ag$_2$S nanowires with an intermediate core–shell nanostructure towards supercapacitor application. New J. Chem. **40**(12), 10144–10152 (2016)
27. H. Xia et al., MnO$_2$ nanotube and nanowire arrays by electrochemical deposition for supercapacitors. J. Power Sources **195**(13), 4410–4413 (2010)
28. S.A. Ahmad et al., Facile synthesis of hierarchical ZnS@ FeSe$_2$ nanostructures as new energy-efficient cathode material for advanced asymmetric supercapacitors. J. Sci. Adv. Mater. Dev. **7**(4), 100489 (2022)
29. J. Ren et al., CoS2 hollow nanocubes derived from Co-Co Prussian blue analogue: high-performance electrode materials for supercapacitors. J. Electroanal. Chem. **836**, 30–37 (2019)
30. L. Wang et al., Hierarchical hollow MoS$_2$ nanospheres with enhanced electrochemical properties used as an electrode in supercapacitor. Electrochim. Acta **186**, 391–396 (2015)
31. P. Christuraj et al., Synthesis and characterization of Zn doped CdS nanoparticles as electrode material for supercapacitor application. Mater. Today Proc. **50**, 2691–2694 (2022)
32. D.S. Patil et al., An all chemical route to design a hybrid battery-type supercapacitor based on ZnCo$_2$O$_4$/CdS composite nanostructures. Curr. Appl. Phys. **20**(12), 1416–1423 (2020)
33. S. Rajkumar et al., Enhanced electrochemical performance of aminophenol-modified ZnO as electrode material for supercapacitors. Ionics **28**(2), 859–869 (2022)
34. S. Portia et al., Facile synthesis of Eu-doped CaTiO$_3$ and their enhanced supercapacitive performance. Ionics **26**(7), 3543–3554 (2020)

35. M.D. Angelin et al., Electrochemical investigation of Zr-doped ZnO nanostructured electrode material for high-performance supercapacitor. Ionics **26**(11), 5757–5772 (2020)

36. A.R. Xavier et al., Synthesis and characterization of Sr-doped CdO nanoplatelets for supercapacitor applications. J. Mater. Sci. Mater. Electron. **33**(11), 8426–8434 (2022)

37. J. Alex et al., Single step auto-igniting combustion technique grown CeO_2 and Ni-doped CeO_2 nanostructures for multifunctional applications. J. Alloy. Compd. **882**, 160409 (2021)

38. R. Srinivasan et al., Enhanced electrochemical behaviour of Co-MOF/PANI composite electrode for supercapacitors. Inorg. Chim. Acta **502**, 119393 (2020)

39. M.D. Angelin et al., Systematic investigation on the electrochemical performance of Cd-doped ZnO as electrode material for energy storage devices. J. Phys. Chem. Solids **161**, 110486 (2022)

40. Z. Tang et al., Fabrication of various metal hexacyanoferrates@CNF through acid-regulation for high-performance supercapacitor with superior stability. Carbon **187**, 47–55 (2022)

41. P. Xu et al., Preparation of porous cadmium sulphide on nickel foam: a novel electrode material with excellent supercapacitor performance. J. Mater. Chem. A **4**(13), 4920–4928 (2016)

42. X. Zhang et al., Morphological control of RGO/CdS hydrogels for energy storage. CrystEngComm **18**(7), 1090–1095 (2016)

43. I. Rathinamala et al., CdS microspheres as promising electrode materials for high performance supercapacitors. Mater. Sci. Semicond. Process. **105**, 104677 (2020)

44. B. Pant, M. Park, S.-J. Park, TiO_2 NPs assembled into a carbon nanofiber composite electrode by a one-step electrospinning process for supercapacitor applications. Polymers **11**(5), 899 (2019)

45. M. Sajjad, W. Lu, Honeycomb-based heterostructures: an emerging platform for advanced energy applications: a review on energy systems. Electrochem. Sci. Adv. **2**, e202100075 (2021)

46. M. Sajjad et al., Recent trends in transition metal diselenides (XSe_2: X= Ni, Mn, Co) and their composites for high energy faradic supercapacitors. J. Energy Storage **43**, 103176 (2021)

47. Z. Zhao et al., Lignosulphonate-cellulose derived porous activated carbon for supercapacitor electrode. J. Mater. Chem. A **3**(29), 15049–15056 (2015)

48. L. Wei et al., 3D Porous hierarchical microspheres of activated carbon from nature through nanotechnology for electrochemical double-layer capacitors. ACS Sustain. Chem. Eng. **4**(12), 6463–6472 (2016)

49. M. Sajjad et al., A novel high-performance all-solid-state asymmetric supercapacitor based on CuSe nanoflakes wrapped on vertically aligned TiO_2 nanoplates nanocomposite synthesized via a wet-chemical method. Journal of Energy Storage **55**, 105304 (2022)

50. K. Khan et al., Development of 1.6 V hybrid supercapacitor based on ZnO nanorods/MnO_2 nanowires for next-generation electrochemical energy storage. J. Electroanal. Chem. **922**, 116753 (2022)

51. M. Pal et al., A facile one-pot synthesis of highly luminescent CdS nanoparticles using thioglycerol as capping agent. J. Nanopart. Res. **14**(6), 1–13 (2012)

52. M. Sajjad et al., Low-temperature synthesis of 3D copper selenide micro-flowers for high-performance supercapacitors. Mater. Lett. **314**, 131857 (2022)

53. M. Sajjad et al., $CuCo_2O_4$ nanoparticles wrapped in a rGO aerogel composite as an anode for a fast and stable Li-ion capacitor with ultra-high specific energy. New J. Chem. **45**(44), 20751–20764 (2021)

54. M. Sajjad, W. Lu, Regulating high specific capacitance NCS/α-MnO_2 cathode and a wide potential window α-Fe_2O_3/rGO anode for the construction of 27 V for high performance aqueous asymmetric supercapacitors. J. Energy Storage **44**, 103343 (2021)

55. M. Sajjad et al., Fabrication of 1.6 V hybrid supercapacitor developed using $MnSe_2$/rGO positive electrode and phosphine based covalent organic frameworks as a negative electrode enables superb stability up to 28,000 cycles. J. Energy Storage **44**, 103318 (2021)

56. S.H. Siyal et al., Free-standing 3D Co_3O_4@NF micro-flowers composed of porous ultra-long nanowires as an advanced cathode material for supercapacitor. Curr. Appl. Phys. **31**, 221–227 (2021)

57. V. Barranco et al., Amorphous carbon nanofibers and their activated carbon nanofibers as supercapacitor electrodes. J. Phys. Chem. C **114**(22), 10302–10307 (2010)

58. M.S. Javed et al., Design and fabrication of highly porous 2D bimetallic sulfide ZnS/FeS composite nanosheets as an advanced negative electrode material for supercapacitors. Energy Fuels **35**(18), 15185–15191 (2021)

59. M. Sajjad et al., Phosphine-based porous organic polymer/rGO composite anode and α-MnO2 nanowire cathode cooperatively enabling high-voltage aqueous asymmetric supercapacitors. J. Energy Storage **40**, 102772 (2021)

60. M. Sajjad, Y. Khan, W. Lu, One-pot synthesis of 2D SnS_2 nanorods with high energy density and long term stability for high-performance hybrid supercapacitor. J. Energy Storage **35**, 102336 (2021)

61. M. Sajjad et al., High energy density asymmetric supercapacitor based on $NiCo_2S_4$/CNTs hybrid and carbon nanotube paper electrodes. J. Mol. Eng. Mater. **7**(01–02), 1950004 (2019)

62. M. Sajjad et al., $NiCo_2S_4$ nanosheet grafted SiO_2@C core-shelled spheres as a novel electrode for high performance supercapacitors. Nanotechnology **31**(4), 045403 (2019)

63. S. Shin, M.W. Shin, Nickel metal–organic framework (Ni-MOF) derived NiO/C@CNF composite for the application of high performance self-standing supercapacitor electrode. Appl. Surf. Sci. **540**, 148295 (2021)

64. J.H. Jeong, Y.A. Kim, B.-H. Kim, Electrospun polyacrylonitrile/cyclodextrin-derived hierarchical porous carbon nanofiber/MnO_2 composites for supercapacitor applications. Carbon **164**, 296–304 (2020)

65. H. Luo et al., Uniformly dispersed freestanding carbon nanofiber/graphene electrodes made by a scalable biological method for high-performance flexible supercapacitors. Adv. Funct. Mater. **28**(48), 1803075 (2018)

66. D.S. Patil, S.A. Pawar, J.C. Shin, Core-shell structure of Co_3O_4@CdS for high performance electrochemical supercapacitor. Chem. Eng. J. **335**, 693–702 (2018)

67. S. BiBi et al., A new ZnO-ZnS-CdS heterostructure on Ni substrate: A binder-free electrode for advanced asymmetric supercapacitors with improved performance. Electrochim. Acta **430**, 141031 (2022)